INSTITUTE OF PHYSICS PUBLISHING MEASUREMENT SCIENCE AND TECHNOLOGY

Meas. Sci. Technol. **12** (2001) 378–394 www.iop.org/Journals/mt PII: S0957-0233(01)16953-5

Forebody and leading edge vortex measurements using planar Doppler velocimetry

Thomas J Beutner[1], Gregory S Elliott[2], Glenn W Williams[3], Henry D Baust[3], Jim Crafton[4] and Campbell D Carter[4]

[1] Air Force Office of Scientific Research, AFOSR/NA, 801 N. Randolph Street, Arlington, VA 22203-1977, USA
[2] Rutgers University, Piscataway, NJ 08855-0909, USA
[3] Air Force Research Laboratory, Air Vehicles Directorate, 2145 Fifth Street, Wright-Patterson AFB, OH 45433-7005, USA
[4] Innovative Scientific Solutions, Inc., Dayton, OH 45440, USA

E-mail: tom.beutner@afosr.af.mil

Received 7 September 2000, accepted for publication 3 January 2001

Abstract

The planar Doppler velocimetry (PDV) technique has been demonstrated by employing it in a large-scale wind tunnel to record velocity fields surrounding a model of a generic fighter plane. The PDV instrument employed here included the following: (i) a frequency monitoring system for measuring the laser frequency corresponding to each set of scattering images; (ii) two detector systems (each composed of two 16-bit CCD cameras), one viewing the model from the top of the wind tunnel and the second from the side; (iii) iodine vapour cells based on the starved-cell design, which eliminated the need for separate temperature control of the iodine reservoir; iv) a vibration-isolated, injection-seeded, Q-switched Nd:YAG laser and (v) custom data acquisition software for linking the four cameras, the laser and the frequency monitor. The PDV instrument was validated by comparing the PDV-derived velocity to the known value in the empty wind tunnel. An error of about 1 m s^{-1} out of an 18.9 m s^{-1} velocity component was found; the image noise component (resulting primarily from the speckle effect) was found to be about 1 m s^{-1}. In addition, as a result of laser-sheet impingement on the model surface, velocities near the model surfaces are biased by background scattering effects. Nonetheless, it has been shown that PDV can be used effectively to map velocity fields with high spatial resolution over complex model geometries. Frame-averaged velocity images recorded at four axial stations along the model have shown the formation of forebody and leading-edge vortices and their complex interaction in the presence of the wing flow field.

Keywords: planar Doppler velocimetry, Doppler global velocimetry, vortex, laser, wind tunnel

(Some figures in this article are in colour only in the electronic version; see `www.iop.org`)

1. Background

1.1. Motivation

The development of complex aerodynamic systems, combined with the development of computational fluid dynamics (CFD), has resulted in widespread interest in diagnostic techniques capable of providing extensive, non-intrusive measurements of complex flow fields. These measurements may serve dual purposes in aircraft design and CFD validation efforts. First, they provide the aircraft designer with details of flow-field

interactions that cannot be obtained from surface pressure and integrated force measurements. Second, they provide detailed flow-field data for comparison to or calibration of CFD methods. In both cases, the ideal measurement technique is non-intrusive—producing no disturbances to the flow field being measured. An ideal technique should also be capable of making measurements of unsteady flow-field interactions. In order to be affordable in large-scale wind tunnels, an ideal technique must provide these measurements in a short test period.

While point-wise techniques, such as laser Doppler velocimetry, provide velocities non-intrusively, a new category of laser-based techniques has emerged which make use of light sheets to provide more extensive data in the flow field, as well as higher data acquisition rates. These range from strictly qualitative techniques, such as laser-light-sheet flow visualization, to quantitative techniques such as molecular flow tagging, particle image velocimetry, planar laser-induced fluorescence, and planar Doppler velocimetry.

A relatively new class of these planar measurement techniques has developed which use molecular or atomic filters in conjunction with cameras and light sheets to interrogate the flow field. These techniques have been associated with several names, each of which identifies some important features of the technique: planar Doppler velocimetry (PDV) [1–9], filtered Rayleigh scattering (FRS) [10–13], Doppler global velocimetry (DGV) [14–27] and filtered planar velocimetry (FPV) [28]. This new class of diagnostic techniques offers the possibility of making non-intrusive, instantaneous velocity measurements over an entire plane in a wind-tunnel flow field. Features of these techniques make them particularly attractive in certain flow regimes and applications.

1.2. Theoretical basis

With PDV, one measures the Doppler frequency shift of light scattered by seed particles (e.g. smoke or condensation) in the flow. The Doppler shift ($\Delta\nu$) is dependent on the incident light wavelength (λ), the velocity of the scattering particle ($\boldsymbol{V}$) and the observation ($\hat{\boldsymbol{o}}$) and incident light ($\hat{\boldsymbol{i}}$) directions (figure 1):

$$\Delta\nu = \frac{\boldsymbol{V}\cdot(\hat{\boldsymbol{o}}-\hat{\boldsymbol{i}})}{\lambda}. \tag{1}$$

Thus, the measured velocity component lies along the bisector of the incident light and observation vectors, and the technique may be extended to multiple-component velocity measurements by observing the flow from more than one direction (i.e., changing $\hat{\boldsymbol{o}}$), or illuminating the flow from more than one direction (i.e. changing $\hat{\boldsymbol{i}}$).

It should be noted that the PDV technique does not depend on resolving individual seed particles or their displacement in the flow field, as is required for the particle image velocimetry (PIV) technique. Since the measurement is based only on resolving the Doppler shift associated with the light scattered off the seed particles, many particles may contribute to the recorded signal. This can be an advantage in large-scale facilities where long viewing distances, non-orthogonal viewing angles and lack of control of seed particles or the presence of condensation may make resolution of individual particles challenging. Since there is no double exposure

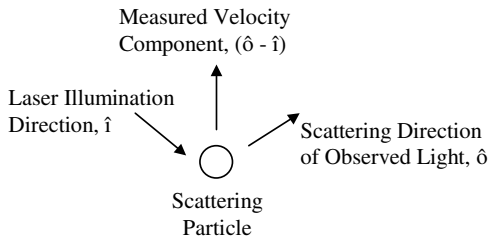

Figure 1. Vector relationships of incident and scattered light and the measured velocity component.

required in the PDV technique, there are no complications presented with particles moving out of the light sheet. This is problem for PIV implementation, particularly when the light-sheet normal and the principal velocity vector coincide. The PDV technique can also be employed for instantaneous measurements [14], limited only by the laser pulse duration or the camera exposure (when using a CW laser); noise from laser speckle, however, limits the precision of individual velocity images in PDV.

The crucial aspect of the PDV technique is that the small frequency shifts associated with the scattered light be resolved. For this measurement, an absorption line of molecular iodine is used. A laser is tuned to a frequency corresponding to an absorption line in the iodine spectrum. The laser is then used to form a light sheet illuminating a planar region of the flow field. Two cameras are used to image this area. One of these two cameras—usually referred to as the signal camera—images the flow through a molecular iodine filter. The intensity recorded on this signal camera is dependent on the frequency of the scattered light and the absorption properties of the iodine filter. The other camera—usually referred to as the reference camera—provides an unfiltered image of the flow field, which may be used to normalize intensity variations due to seeding density and the laser energy distribution. By using multiple camera pairs, each observing the flow from a different direction, it is possible to extend this technique to make multiple-component velocity measurements over an entire plane of the flow field.

1.3. Developmental history

Two recent reviews provide details of the development of filter-based velocimetry systems. The first, by Elliott and Beutner [29], provides details of the early development of filter-based techniques and examples of the range of applications for which these techniques have been used. The second, by Samimy and Wernet [30], provides selected descriptions and examples of both PDV and PIV measurement techniques.

Initially Shimizu *et al* proposed the use of molecular and atomic filters for light detection and ranging (LIDAR) applications. Here, the purpose of the molecular filter was to block transmission from particle scattering, while passing the thermally broadened scattering from molecules [31, 32]. Two groups of researchers, Komine and coworkers, and Miles and coworkers, independently introduced the use of molecular filters to flow diagnostics at approximately the same time—each receiving patents on their concepts. Komine *et al* developed a technique in response to a request to measure air velocity in a wind-tunnel test. They proposed that the

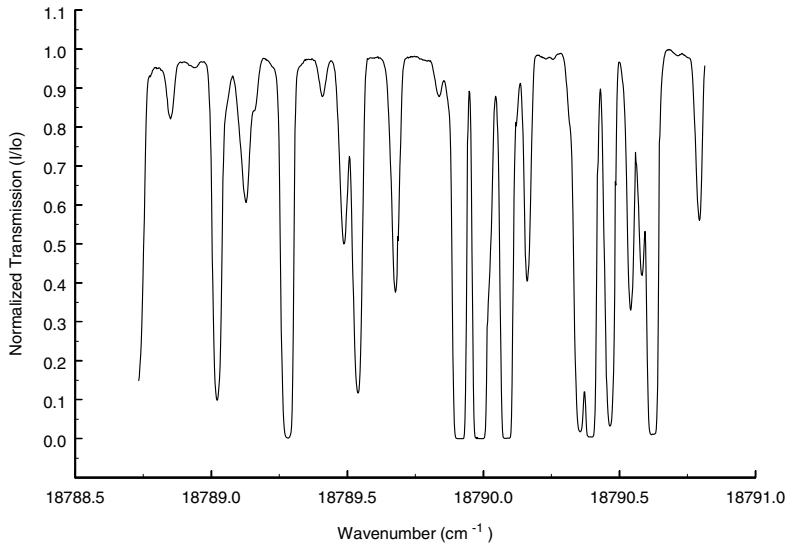

Figure 2. Experimentally measured iodine absorption spectrum showing tuning range of the frequency-doubled Nd:YAG laser.

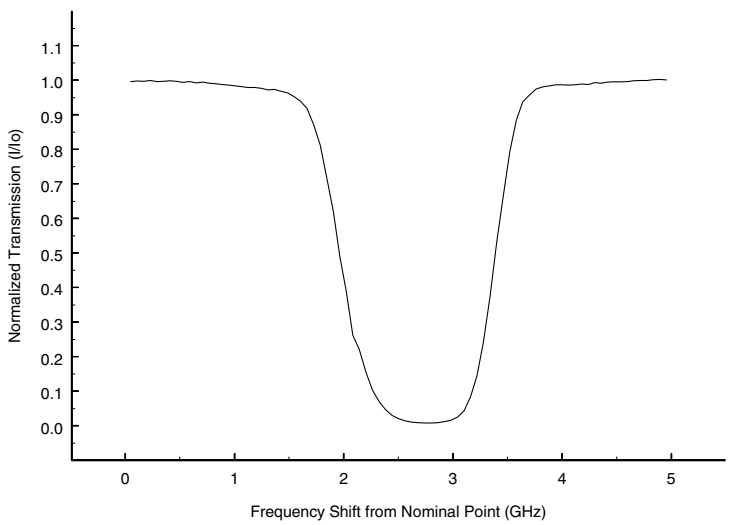

Figure 3. Absorption line used in these experiments. This line is at approximately 18 789.28 cm^{-1}.

transmission through a molecular filter be used to measure the Doppler shift of light scattered from seed particles in the flow. Techniques based on an iodine filter and either an argon-ion laser or an injection-seeded Nd:YAG laser were proposed [15, 16]. In the initial implementation of this idea, the transmission was determined by analogue division of two camera signals, one of which viewed the flow through the iodine cell and the other of which viewed the flow directly. These early tests required pixel-to-pixel alignment between the cameras and encountered difficulties due to camera noise, laser frequency drift and other systematic problems. In later collaborative projects with NASA researchers, Komine and Meyers [17] developed much of the conceptual framework for many of the signal processing algorithms used by a variety of researchers today. Miles *et al* [13] initially concentrated on the use of filter-based techniques to improve flow visualization and background rejection in cases where signal is low and can be obscured by background scattering. These efforts were later extended to quantitative imaging techniques. Again, the first demonstrations were made using a molecular iodine filter [10–13].

Considerable advancements to the signal processing and procedures, systematic error analysis, applications in large-scale facilities, component characterization and hardware development have been made by university and laboratory groups [29, 30]. Many of these advancements are reflected in the experimental design outlined here. As the accuracy and precision of the PDV technique has improved, it has evolved into a technique that may be used to investigate complex flows in large-scale facilities. Early systems based on analogue normalization [15] have been largely replaced by systems using scientific-grade cameras. Signal processing has been addressed by several researchers, each with a slightly different approach. Most processing procedures now include steps to overlay the images with tie points, steps to calibrate cameras with flat-field images, steps to remove background illumination, low-pass filtering to reduce speckle noise and careful *in situ* calibration of the

iodine cells. Laser frequency stabilization and monitoring has been widely recognized as an important aspect of error reduction. Speckle noise has also been addressed both in system design and image processing [3, 9]. Iodine spectrum predictions [12] have been used by many researchers in calibrating and testing their lasers. A variety of optical arrangements have been tested in an effort to address signal levels, polarization sensitivities, angular dependence of Mie scattering, system cost and optical access. These systems have included side-by-side camera systems [26, 33–35], single-camera split-image systems [3, 6, 36], a colour-camera-based system [37], and two-camera arrangements with a beam splitter [2, 4, 14, 20–23]. Many of the original investigations of PDV have centred on measurements of a known velocity field—often a jet flow or rotating wheel—in an attempt to assess system performance. As the PDV technique has matured, it has been applied with greater accuracy to increasingly complicated flow fields [4, 14, 21, 23, 24, 27].

2. PDV system

2.1. Laser system

An externally water-cooled, frequency-doubled Nd:YAG laser ($\lambda = 532$ nm) was used in these experiments. The short-duration pulse of the Nd:YAG laser ($\sim$10 ns) allowed unsteady flows to be investigated, though in this paper we present only the frame-averaged images. This laser was capable of delivering approximately 320 mJ per pulse at 10 Hz [38], and was operated in single-frequency mode by using a seeding laser diode [39]. The laser frequency was controlled by means of a bias voltage applied to the laser diode seeder, allowing fine tuning of the laser frequency over a broad tuning range (figures 2 and 3). This fine control was useful not only for adjusting the laser to the desired point on the iodine absorption line, but also for experimental determinations of the absorption line shape.

The Nd:YAG laser has a linewidth of $\sim$100 MHz (consistent with a transform-limited 10 ns pulse duration) and exhibits pulse-to-pulse variations of approximately 10 MHz as a result of the dither mechanism used to match the seeder frequency to one of the Nd:YAG cavity modes. When operating this laser in harsh wind tunnel environments, one may observe (i) drift of the set-point frequency, in response to large ambient temperatures variations, and (ii) large pulse-to-pulse frequency variations (e.g., $\pm$40 MHz) and/or multi-longitudinal-mode operation, in response to significant acoustic noise and wind-tunnel vibration. Of course, vibration problems are exacerbated by the need to mount the laser optical table to the wind tunnel superstructure.

These problems were mitigated in these experiments by (i) controlling the temperature of the surrounding environment by surrounding the test section with a tent and air-conditioning this region and (ii) floating the platform on which the laser was mounted with actively controlled pneumatic feet. Relative to our previous implementation of PDV in the Subsonic Aerodynamic Research Laboratory [4, 23], this arrangement greatly reduced the number of unseeded (multi-mode) laser pulses and the magnitude of the pulse-to-pulse frequency fluctuations. Monitoring the nominal operating frequency of the laser on a pulse-by-pulse basis was still necessary to mitigate residual frequency drift and pulse-to-pulse variations. Note that one negative consequence of floating the laser platform is that the laser beam could be inadvertently steered with respect to the tunnel, due to tunnel vibration or through an operator placing weight on the laser table.

As noted above, the laser produces a multi-mode pulse when the seed laser frequency does not correspond to a cavity mode. Multi-mode lasing is characterized by an increase in the so-called laser-pulse-build-up time and by a temporal intensity profile with multiple lobes that results from beating of the cavity modes. Of course, these pulses are unacceptable for use with the PDV technique since they are composed of multiple laser frequencies. The build-up time is substantially reduced when single-mode operation is achieved (typically by $\sim$10 ns for this laser), and the seeder system employs a photodiode-timing circuit in its control of the seeder system. The seeder system converts the build-up time into a voltage, which was monitored on a pulse-to-pulse basis in this experiment, providing a simple means of discriminating against multi-mode laser pulses. Only images with corresponding build-up time voltages below a threshold level (indicative of a single-mode laser pulse) were saved by the data acquisition system.

Similar monitoring procedures were used when calibrating the absorption profiles of the individual iodine cells. In this case, many of the temperature and vibratory problems were eliminated since the frequency scans were performed during a short time period with the tunnel off. All the iodine cells used in the experiment were calibrated simultaneously. A delay was incorporated after each laser frequency change during the scans to allow the laser to stabilize on the new seeder frequency. Additionally, the laser was monitored for single-mode operation, with the requirement that 50 sequential laser pulses be single mode before recording the data point and incrementing the seed laser frequency.

2.2. Optical setup

A schematic diagram of the optical setup may be seen in figure 4. As noted above, the laser and frequency monitoring system were placed on an optical breadboard that was mounted on top of the wind-tunnel superstructure. The light sheet origin was thus above the tunnel ceiling, on the tunnel centreline, and was inclined to produce a light sheet that was nearly normal to the model axis (see section 3). A two-component PDV system was used. The detector systems were placed upstream of the light sheet with one viewing the light sheet from the top of the tunnel, on the centreline, and the other viewing the light sheet from an upstream side window. To produce acceptable signal levels and intensity discrimination in the wind tunnel, four 16-bit scientific-grade CCD (charge-coupled device) cameras were used, each with an array of 512×512 pixels (each 24 μm square) [40]. Each camera was fitted with an identical 105 mm $f/2.8$ lens (operating at full aperture) and a bandpass filter composed of two colour-glass filters. The purpose of the bandpass filter was to reduce the influence of background lighting variations; furthermore, the cameras were fitted with integral mechanical shutters, which were typically opened for 50 ms around the laser pulse. Each pair of cameras, signal and reference, was controlled by a personal computer (PC); the

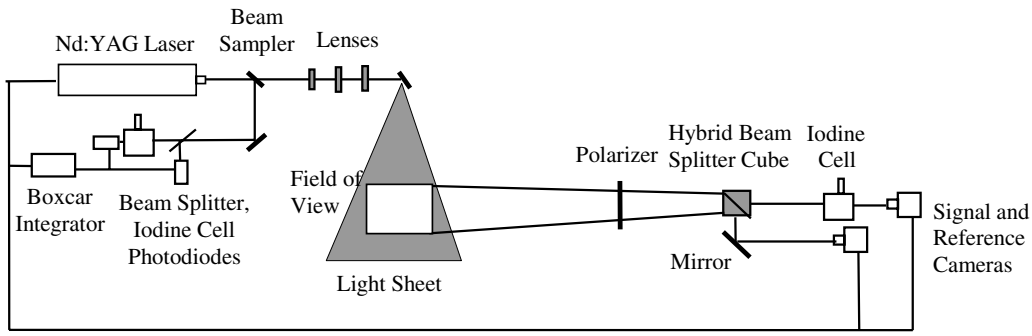

Figure 4. Schematic diagram of optical setup.

two PCs were then linked through a local area network (using ethernet computer cards). The two PCs, four CCD cameras, gated integrators and laser control were integrated with custom C-language-based software using the National Instruments LabWindows/CVI package. The two computers were then operated in a master/slave configuration. The master computer was used to control the experiment: it collected images from all cameras and voltages from the frequency monitoring system and laser seeder (for measurement of build-up time) and sent voltages to the seed laser to control its frequency. A digital delay generator was also employed to supply trigger pulses to the laser (at a 10 Hz frequency) and the data acquisition system.

A hybrid beam-splitting cube (76 mm on a side) was placed between the signal and reference cameras to ensure that each camera viewed the flow field from a nearly identical angle, thus minimizing the possibility of bias errors due to angular variations in scattering intensity and polarization. The hybrid cube is designed to minimize the sensitivity of the beam splitter to the polarization of the incoming light [41]. In addition, a polarizing element placed in front of the beam splitter ensured that only one polarization component would be received by the cameras. Separate cameras were used for the signal and reference images to eliminate the possibility of optical cross-talk between the signal and reference images which can occur when a 'split-image' system is used to record both signal and reference images on a single CCD array. While a two-camera system is obviously more costly than a single-camera system, this cost must be weighed against the considerable run-time cost for operation of a large-scale wind tunnel.

2.3. Laser frequency monitor

As noted earlier, pulse-to-pulse monitoring of the laser frequency is necessary, particularly in harsh operating environments. Pulse-to-pulse RMS frequency variations of about ± 40 MHz were observed in our initial wind-tunnel tests [4], even in the laboratory, we observed frequency variations of ± 10 MHz. In either case, these frequency variations can degrade the accuracy of the measurements, especially at low velocities (e.g. 10 m s^{-1}). To monitor the laser frequency, we measured the transmission of a reference iodine filter using high-speed photodiodes [42] and a gated integrator system [43]. Here, a small portion of the laser beam was split off, expanded—to avoid transition saturation effects—and then split a second time; one of these two beams was directed through the reference iodine cell and then to a photodiode, while the other was sent directly to a second photodiode. Each expanded beam was then focused on a flash-opal diffuser placed before the respective photodiode. This arrangement made the frequency monitor less sensitive to variations in optical alignment and ensured that the photodiode sampled the entire beam. An electrically actuated shutter system, controlled by the data acquisition software, was also placed in the frequency monitor beam path and was closed prior to data image collection, allowing the measurement of baseline gated-integrator voltages. The photodiode voltages were recorded and digitized with 12-bit resolution (on a 10 V range), and from these voltages we inferred the laser frequency. Thus, the frequency monitor could be used to provide real-time feedback on the laser frequency, allowing the laser to be tuned to the desired point on the absorption curve. In addition, photodiode voltages were recorded synchronously with each set of camera images so that each could be tagged with a laser frequency. Included in the frequency monitor system were stations for two additional iodine cells (complete with photodiodes and gated integrators). This was done so that all three iodine cells could be calibrated simultaneously. Note that while the laser was pneumatically isolated (on a separate platform), the frequency monitor was not. An unintended consequence of this design was that the frequency monitor proved to be susceptible to beam steering effects.

2.4. Iodine cell

The iodine cell was a critical component in this system, and the absorption profile of the iodine cell must be known and stable in order to accurately determine the Doppler shifts. The iodine cells were constructed with large cylindrical cell bodies and small protruding cold fingers, as shown in figure 5. The cells used in this experiment had a diameter of 76 mm and a length of 203 mm. The signal camera viewed the flow through the cell body, which had optical windows on both ends of the cylinder.

These cells used a starved-cell design, meaning that no crystalline iodine was present in the cells during operation. The starved-cell design is preferred over a saturated-cell design, because it eliminates the absorption line sensitivity associated with cold-finger temperature variations and the need for temperature control of the cold finger during the test. The starved cells were created by first placing crystalline iodine in

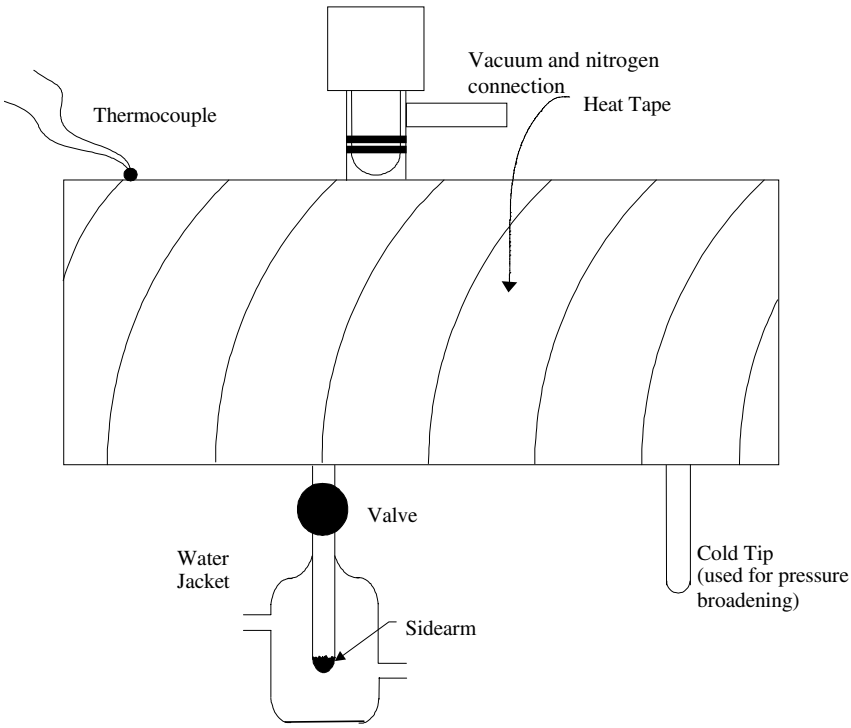

Figure 5. Iodine cell schematic diagram.

the cell, and then evacuating the cell using a vacuum pump attached to the cell body. The stopcock on the vacuum pump attachment was then closed, and the cell was brought to an equilibrium operating condition with the cell body at 378 K and the cold finger at 313 K. After stable operation was achieved, all crystalline iodine in the cell was in the cold finger. At this point a valve was closed, sealing off the cold finger. The result of this process is a cell in which no solid iodine is present in the cell body during operation. The cell absorption characteristics are relatively insensitive to the temperature of the cell body, but in a saturated cell they are very sensitive to variations in the cold-finger temperature [1, 12, 26, 44]. At this point, the cell may also be pressure broadened, to tailor the absorption line characteristics. To pressure broaden the cell, a cold tip on the cell body was cooled in a bath of acetone and dry ice, causing the iodine in the cell to condense at this location. Nitrogen was then introduced into the cell through the valve system described earlier, after first using the vacuum pump to purge all air from the plumbing system. The pressure-broadened cell is characterized by a shallower absorption line slope. This effectively extends the range of frequency shifts that may be measured by the system [33]. In the case of the laser frequency monitor, there was no need for pressure broadening; rather, more sensitivity to laser frequency was desired. A small amount of pressure broadening (approximately 700 Pa) was used with both camera systems to allow measurements of a larger range of velocities. Although actual measured velocity ranges were within the measurement range of an unbroadened cell, the use of a broadened cell allowed greater flexibility in the experimental setup, without prior knowledge of the actual velocity range.

As noted above, all iodine cells were calibrated simultaneously by splitting the laser beam and passing it through each cell and then monitoring the absorption of each cell with photodiodes and gated integrators. By tuning through several absorption lines in the iodine spectrum and then comparing to a calculated spectrum [12], we calibrated the frequency axis (MHz V^{-1}) and confirmed that this calibration factor was constant within the frequency range of interest. This overall tuning range can be seen in the experimentally measured iodine transmission spectrum shown in figure 2. The broad tunability of the Nd:YAG laser allows selection from several distinct absorption lines. The line chosen for use in these experiments is in the vicinity of 18 789.2 cm^{-1}. A more detailed plot of this absorption line (without pressure broadening) may be seen in figure 3. The edge of this iodine absorption line had a useable width of approximately 600 MHz. For the optical configuration used here, a 1 m s^{-1} velocity change corresponded to a frequency shift of $\sim$3 MHz; of course, this number varies slightly for each detector location and laser-sheet orientation. This gives a total measurable velocity range of approximately 200 m s^{-1}. Additional pressure broadening of the iodine cell could be used to increase the range of measurable velocities with this instrument, if needed, but this naturally comes at the cost of reduced sensitivity to transmission.

2.5. System operation

For a normal operation of this system, the laser frequency is tuned to the centre of one side of the iodine absorption line. When light is scattered by moving particles, it is Doppler shifted, as per equation (1). Shifts in the frequency of the scattered laser light show up as intensity variations after normalization by the reference-camera image. In practice, if large frequency shifts are expected in only one direction (for

example, when the velocity field is biased by the freestream velocity), then the laser may be tuned to a higher or lower transmission point on the absorption curve in order to capture large positive or negative shifts.

Routine checks on the system operation were made before, during, and after all runs. Tuning the laser out of the absorption line to a relatively 'flat' portion of the iodine absorption spectrum results in measurements that are insensitive to velocity shifts. This was used as a check, both on-line and in post-processing, to ensure the system was operating as expected. Background illumination varied because of model location and the amount of sunlight transmitted through the wind-tunnel diffuser and inlet. Background images were thus taken with each data set throughout the run. Furthermore, images were recorded using reduced laser power to provide the model location and the laser-sheet impingement point within the field of view. To ensure stable operation of the iodine cells and laser, the iodine cells were calibrated with a frequency scan at the beginning and end of each day. These scans were compared to check for any variations in laser or iodine-cell performance. In addition, each cell was periodically checked for iodine condensation on the cell windows. The dot-card images were recorded at the beginning and end of each day to check for any movement of optical components which could cause shifts in images.

In total, about two-thirds of both the recorded images and the total test time was devoted to calibration. Some systematic improvements, such as the use of permanently sealed starved iodine cells—where the cell stem is welded off and the valve removed—may considerably reduce the time required for calibration during each test day. Other calibration steps, such as pixel calibration using an integrating sphere and *in situ* scattering off 'stationary' smoke, have been eliminated as system performance has been checked and potential concerns addressed.

2.6. Data processing

Multiple steps are required to process the PDV data. As the technique is based on intensity measurements, care must be applied throughout the processing to preserve the accuracy of the intensity measurements on a pixel-by-pixel basis. First, background images were subtracted from data images to remove stray light illumination and dark current. Letting the data images be denoted by R_D and S_D, for the respective reference and signal cameras, and the background images be denoted by R_B and S_B, for the respective reference and signal cameras, then R'_D and S'_D are data images corrected for background illumination and dark current:

$$R'_D = R_D - R_B \tag{2}$$

$$S'_D = S_D - S_B. \tag{3}$$

Flat-field corrections were also performed to account for optical efficiency differences between the two cameras and their respective optics. For these calibrations, the laser beam was expanded, passed through an optical diffuser and then directed onto a white card placed in the position of the original light sheet. The laser was tuned outside the absorption curve in order to obtain a flat field that was characteristic of the maximum transmission ratio that would be measured by the signal and reference cameras in data images. The transmission through the reference iodine cell was also recorded with these images and was used to normalize the reference iodine-cell transmission profile in a manner consistent with the normalization of the data images. It is not necessary for the illumination used in these flat-field corrections to be perfectly uniform. Since the flat-field correction is used only for a frequency-independent camera-to-camera correction, the process of ratioing the signal- and reference-camera images will remove variations in the illumination of the card. Intensity variations with a high spatial frequency—resulting, for example, from laser speckle—may still not cancel perfectly in the ratioing process; however, speckle noise, in particular, was reduced by use of an optical diffuser. A series of images, R_G and S_G for the reference and signal cameras, respectively, were recorded and averaged for these flat-field corrections. Background (laser-off) images were also recorded here and subtracted from the laser-on images to produce the corrected flat-field images:

$$R'_G = (R_G - R_{GB}) \tag{4}$$

$$S'_G = (S_G - S_{GB}). \tag{5}$$

Low-pass filtering was performed on the images using a rolling 5×5 pixel digital filter. All pixels were weighted equally in a 5-pixel-square cell in the image, and the average value was assigned to the central pixel. This filtering effectively reduces the spatial resolution of the images, resulting in a measurement field containing about 100×100 independent measurements. This process was applied to the data images, resulting in filtered images R''_D and S''_D, and to the flat-field correction images, resulting in filtered images R''_G and S''_G. The purpose of this filtering step was to reduce speckle noise. For the time-averaged measurements shown here, averaging images also reduces the speckle noise. Of course, other filter kernels, for example based on a Gaussian function, or pixel binning could also be used in this step. Various filter kernel sizes have been investigated [14], and speckle noise is generally reduced as larger kernels are used. For the optical setup used in these experiments, estimates were made of the total RMS uncertainty due to seeding variations and speckle in the raw data images, and showed respective RMS uncertainties of 9%, 5% and 3% when no filtering, 3×3 filters and 5×5 filters were used. Note that this uncertainty includes both seeding variations and speckle and that the seeding variations will tend to be normalized by the use of the reference image. However, these estimates provide an indication of the effect of spatial filtering on the data. Since both larger spatial filters and increased numbers of averaged images will reduce the noise due to speckle, a trade-off must be made between image resolution, tunnel run-time and acceptable noise levels in choosing the filter size and number of images taken. A 5×5 filter was deemed sufficient, in this case, to demonstrate the efficacy of this technique in a harsh wind tunnel operating environment.

Smith [9] and McKenzie [3] have both investigated speckle noise in similar implementations of the PDV technique, and have made specific recommendations regarding f-number, pixel size and fill-factor, magnification and pixel

binning to reduce speckle. Practical considerations in this case, such as optical access limitations, desired field of view and available cameras determined some of the system parameters used here. For the current test, the CCD array was of the back-illuminated type and thus had a fill factor of 100%; the pixels too were relatively large at 24 μm, and these two factors helped in speckle mitigation. The lenses used here had a moderately fast aperture, with an indicated f-number of 2.8. A faster lens with the same focal length might have been used in this experiment (for example, lenses with the same focal length and an indicated f-number of 1.8 are commercially available), but image blurring might have been problematic, especially with the side-mounted detector system. In addition, speckle may also be reduced by time averaging data. This was accomplished in this case by averaging multiple images acquired with a pulsed laser but may also be achieved by using a CW laser and a long camera exposure [24, 25].

Note that the use of a 5×5 low-pass filter and the cameras used in this implementation of PDV results in a number of independent velocity measurements which is comparable to the value that can be obtained with the digital PIV technique. However, as noted above, PIV can be difficult to apply here due to several complicating factors: poor control of seed density and condensation in the test section, high through-plane velocities, large fields of view and object distances and non-orthogonal viewing angles [45].

As part of the filtering process, pixels with intensity values above or below set thresholds were identified. Pixels with intensity values (after subtracting background images) of less than 500 counts and pixels with intensity values greater than 64 000 counts were marked. These pixels were considered to be too close to the background level or saturation level to be used in the data processing. During the low-pass filtering, the central pixel was marked as bad if any of the pixels in the 5×5 cell were above or below the set thresholds. After being identified, these pixels were not used in any subsequent processing step.

The data from the signal and reference cameras must also be mapped into overlying images. This was accomplished using an image of a dot card that was placed in the data plane. This dot card had uniformly spaced square dots on a sheet of Mylar drafting film which covered the field of view. A legend on the dot card also allowed an absolute reference for position of the card centre. The drafting film was translucent, allowing the dots to be viewed from either side of the card—an essential feature when this technique is extended to viewing angles on more than one side of the light sheet. A robust algorithm was used to determine the centroid of each dot recorded in the camera images. This algorithm detected a dot edge based on a user-defined variation in pixel intensity. The algorithm then traced the edge of the entire dot and found the centroid of the dot based on a weighted average of the inverse of the pixel intensities. The dot centroid locations were used to perform a bilinear interpolation of the raw images into overlying images. This mapping procedure simultaneously eliminated perspective distortions and any magnification differences from the images. This procedure was performed on the data images and the flat-field correction images, resulting in corrected data images, R_D''' and S_D''', and corrected flat-field images, R_G''' and S_G'''.

The next step in the processing procedure was to determine the transmission through the iodine cell for the signal camera. The transmission was determined by dividing the corrected signal- and reference-camera images, and normalizing by the flat-field images. The resulting image, TR, gives the pixel-by-pixel variation in the transmission of the iodine cell for the recorded scattering:

$$\mathrm{TR} = (S_D'''/R_D''')(R_G'''/S_G''') \tag{6}$$

In this step, the top 10% and bottom 10% of the transmission profile were not used, since the transmission–frequency sensitivity falls off in these portions of the profile. Measurements corresponding to these transmission ratios were marked and subsequently not used. This image, combined with a lookup table of the iodine cell transmission profiles and the laser frequency (derived from the frequency monitoring system) on each pulse, gives the frequency shift of the scattered light on a pixel-by-pixel basis. Use of equation (1) allows this information to be transformed into a velocity map of the flow field.

As a final step in the data processing, averaging of the data from multiple images was performed. In addition to reducing speckle noise, averaging of the data also filled in regions in the field of view where the signal levels in individual images was too low due to inconsistent seeding. Note that for pulsed lasers, due to the pulse-to-pulse variations in laser frequency, averaging of images from multiple laser pulses may only be achieved after data from each individual pulse is processed and reduced to frequency shifts.

3. Wind tunnel and model

This test was conducted in the Subsonic Aerodynamics Research Laboratory (SARL) wind tunnel at the Air Vehicles Directorate of the Air Force Research Laboratory. The SARL wind tunnel is an open-circuit, low-speed tunnel with a 3.05 m $\times$ 2.13 m test section. A unique feature of the SARL wind tunnel is the axial translation capability of the model support. In addition to articulation for pitch, roll and yaw, the model support may move axially up to 203 mm. This allows multiple data planes to be studied with a single optical setup by moving the model through the light sheet. Over 50% of the test section walls are made of optical quality Plexiglas, allowing a wide range of viewing angles. However, at the time of this test, only two of the Plexiglas windows (located on top of the SARL) had windows suitable for transmitting a pulsed-laser beam. These windows included a sapphire window insert through which the beam was transmitted.

Two experimental cases were considered in the present work. An empty-tunnel test was performed to validate the system performance. For this case, the model was removed from the wind tunnel and the freestream velocity was measured with the PDV instrument. This provided a known, uniform velocity field that was most representative of the conditions for which model data was collected, with vibrations and particle scattering similar to the case with the model in place. These results were used to assess system accuracy and provide validation of the PDV instrument. One remaining difference, however, is the presence of secondary scattering off the model

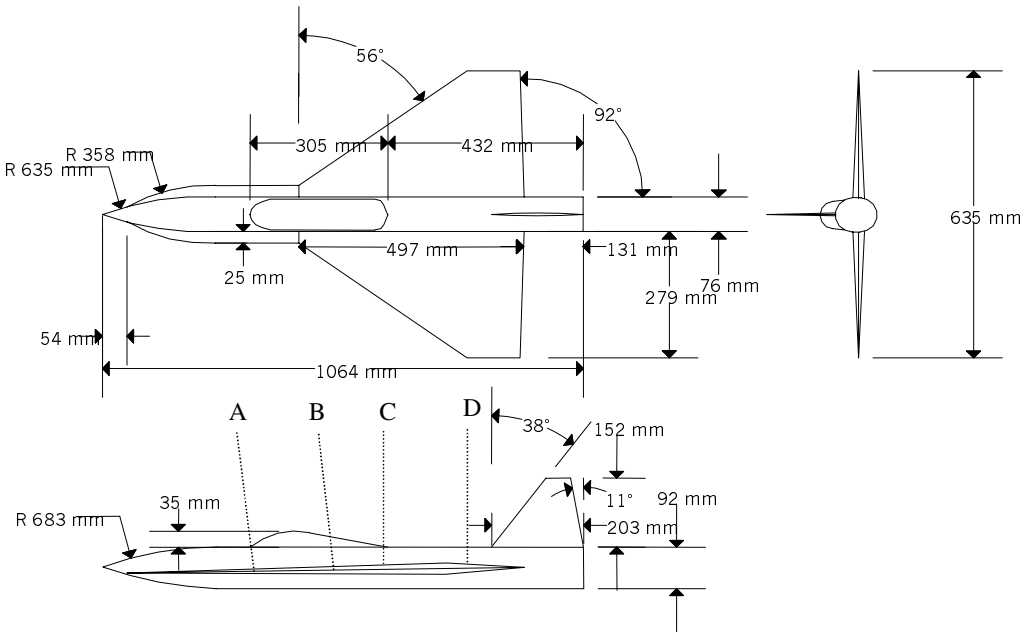

Figure 6. 56° delta wing schematic diagram. PDV measurement planes are shown as dotted lines.

surface, which is not present for the empty tunnel. The effects of secondary scattering can be observed in the data set as 'ghost' images of the model surface as seen through the light sheet, and as saturation regions where direct reflections off the model surface caused local saturation in the camera. The empty-tunnel experiments are summarized here as they relate to system error analysis.

The second experimental case presented here includes measurements of a strake vortex and wing vortex system on a generic fighter configuration (figure 6). This model had a 90° strake, a 56-degree wing sweep and a realistic body, including a canopy and vertical tail. Although these geometric features are typical of fighter aircraft, this model is generic in that it does not correspond to any actual or planned aircraft configuration. This model had previously been used in flow visualization studies to examine the interaction of strake and leading-edge wing vortex systems. Although generic in design, this model develops many of the flow features typical of fighter configurations, including strong strake- and wing-vortex systems. This model also presents challenges to optical measurement techniques, such as model and body curvature and the presence of a tail—both of which may limit viewing or interrogation angles or result in unwanted surface reflections. This model was tested at an angle of attack of 23° and a Mach number of 0.2 (69.2 m s^{-1}).

Light sheets used in the PDV measurements intersected the model at four locations. The forward two locations corresponded to positions 108 mm forward of the wing/strake junction and 76 mm downstream of the wing/strake junction. For these two locations, the light sheet was inclined 83° to the model body axis, with the top of the light sheet tilted 7° upstream of the plane normal to the model axis. This was necessary because of limited optical access for the laser beam, as noted above. The aft two locations corresponded to positions aligned with the trailing edge of the canopy and with the leading edge of the wing tip. At these aft locations, the light sheet was aligned normal to the body axis.

4. Uncertainty analysis and validation measurements

Since this technique is based on making intensity measurements in order to determine frequency shifts, there are a variety of error sources which may lead to biases or random uncertainties in the data. Following the uncertainty analysis of Mosedale *et al* [4], where the analysis of a similar system is given, the Doppler shift equation (equation (1)) may be written in scalar form as

$$V \cos \Omega = \frac{\lambda \Delta f_D}{2 \sin(\phi/2)} \tag{7}$$

where ϕ is the angle between the laser propagation direction and the scattering direction and Ω is the angle between the velocity vector and the PDV system sensitivity direction. Notice that the left-hand side of this equation contains the directionality of the velocity vector. The only geometrical relation contained in the right-hand side is independent of the velocity field. We may view the left side, including the cosine term, as the quantity to be measured which is the velocity parallel to the system sensitivity direction ($V_{\|}$) and include the error associated with Ω only when comparisons are made with the freestream velocity.

In this analysis, we consider conditions characteristic of the top-mounted detector system; furthermore, to make the analysis more tractable, we consider a local-linear fit to the transmission profile with associated slopes and intercepts, and we write equation (7) in terms of measured quantities. This approach to solving for the uncertainty allows the individual sources of uncertainty to be separated, calculated, and compared in a simplified fashion. Note that the purpose here is to guide us in understanding which are the dominant

Table 1. Average parameter uncertainty averaged over typical operating range.

Independent variable	Uncertainty in independent variable		Resulting velocity error (m s^{-1})	
	Bias	Random	Bias	Random
ϕ	6°	—	1.6	—
m_c (GHz/trans)	0.0041	0.000 11	0.69	0.02
b_c (GHz)	0.0016	0.000 34	0.50	0.10
$\Delta S_1/S_1$	—	3.6%	—	2.5
$\Delta S_2/S_2$	—	3.6%	—	2.5
m_{cal}	0.0052	—	0.34	—
$\Delta S_3/S_3$	—	0.25%	—	0.22
$\Delta S_4/S_4$	—	0.1%	—	0.09
m_r (GHz/trans)	0.0041	0.000 11	0.87	0.02
b_r (GHz)	0.0016	0.000 34	0.50	0.10
Total			2.3	3.5

error terms, rather than to predict with certainty the PDV error. The linearized relationship for $V_\parallel$ is given by

$$V_\parallel = \frac{\lambda}{2\sin(\phi/2)}\left[m_c\frac{S_1}{m_{cal}S_2 + b_{cal}} + b_c - m_r\frac{S_3}{S_4} - b_r\right] \quad (8)$$

where S_1 and S_2 are the respective intensities from the signal and reference cameras, S_3 and S_4 are the respective intensities from the signal and reference photodiodes in the laser frequency monitor, m_c and b_c are the respective slope and intercept of the linearized frequency function for the camera, m_r and b_r are the respective slope and intercept of the linearized frequency function for the laser frequency calculation and m_{cal} and b_{cal} are the respective slope and intercept associated with camera intensity calibrations. Expressing the uncertainty in the velocity according to standard error propagation methods,

$$\Delta V = \left\{\sum_i \left(\frac{\partial V}{\partial x_i}\Delta x_i\right)^2\right\}^{1/2} \quad (9)$$

where the x_i are the independent variables seen in equation (8).

Table 1 gives the average estimated uncertainties, categorized as either bias or random uncertainties, in each of the independent variables and the resulting total. For purposes of assessing the uncertainty, the range of laser set points and the measured frequency shifts actually used in the experiments were considered. These set points and frequency shifts were used to estimate the slopes and intercepts of local-linear fits to the iodine transmission profile. The reported uncertainties in velocity represent an average of these estimates. Since the uncertainties obviously depend on the local slope of the transmission profile, this gives a method of approximating velocity-dependent and laser-set-point dependent system errors, since both these effects may cause frequency measurements to be made in portions of the iodine absorption profile where transmission–frequency sensitivity is lower. Here, the contributions due to the wavelength of the laser (λ) and b_{cal} have been neglected since they were found to be much smaller than the other sources of uncertainty. The first uncertainty listed in this table is that in ϕ, the angle between the laser propagation direction and the scattering direction. This measurement contains uncertainties associated with the measurement of the central angle, as well as uncertainties associated with the variation of this angle across the field of view. For the current arrangement, the variation of this angle across the field of view dominated and was determined to have a maximum variation of $\pm 3°$ from the average value. This uncertainty leads to a bias error since it does not change during the run (assuming the camera and laser systems remain stationary).

The linearized frequency functions are the next sources of uncertainty listed. These functions are taken as the linear portion of the iodine transmission profile and are described by the slopes and intercepts of the filter transmission function for the camera (m_c and b_c) and the frequency monitoring system (m_r and b_r). The slopes and intercepts lead to both bias and random uncertainties because they may not have been measured accurately initially, and they may vary slightly during the course of an experiment. For the frequency monitoring system, the bias error is suspected to be due primarily to uncertainties associated with the reference photodiode, which was later found to be affected by slight beam steering (resulting from having the laser and frequency monitor on different surfaces). The bias uncertainties for m_r and b_r reported in table 1 are based on repeated measurements made during the wind-tunnel test. The random uncertainty in m_r is due to variations of the cell body temperature only, since starved iodine cells are used. From previous work we estimate the sensitivity of m_r to cell-body temperature was 0.21 MHz K^{-1} and that the cell-body temperature varies by about ± 0.5 K, resulting in an uncertainty of about ± 0.1 MHz in m_r [4]. Likewise, we estimate that the sensitivity of b_r to cell-body temperature is 0.68 MHz K^{-1}, resulting in an uncertainty of ± 0.34 MHz in b_r. Similar arguments can be made for the slope (m_c) and intercept (b_c) of the frequency function used in the camera system.

Next to be considered is the uncertainty associated with the intensities of the signal and reference cameras. These uncertainties will be regarded as random since the majority of the contribution to bias is associated with the optical and electronic calibration. The noise-to-signal ratio (e.g. $\Delta S_1/S_1$) was relatively constant with intensity; this is a characteristic of speckle-dominated noise [3]. For the empty-tunnel experiments, the noise-to-signal ratio of the signal and references images is approximately 3.6% after low-pass filtering. Another source of random uncertainty in intensity is associated with the photodiodes in the frequency monitoring system. The major source of uncertainty is random and is

Table 2. PDV errors for Mach 0.2 tunnel operation and -18.9 m s^{-1} velocity component.

	Bias error (m s^{-1})	Random error (m s^{-1})
Instantaneous image	1.5	0.95
Average of 130 images	1.0	0.35

approximately equal to the bit-count resolution of the A/D conversion, which is 2.5 mV. This results in a random error of $\Delta S_3/S_3 \approx \pm 0.25\%$ and $\Delta S_4/S_4 \approx \pm 0.1\%$ assuming typical values of $S_3 \approx 1$ V and $S_4 \approx 2.5$ V; of course, this probably represents a 'best case', and the true values may be larger. The final source of uncertainty is associated with the camera calibration. In this regard the cameras are assumed to be linear in their response. Estimates of the uncertainty associated with the camera calibration procedures, m_{cal}, are based on previously reported work in which illuminations were varied and camera response was calibrated [4].

Along with the average uncertainties in the velocity due to uncertainties in each of the independent variables, the average total uncertainty in the velocity combining all these sources is given in table 1. Note that the total uncertainty is in fact not constant, but varies with the set point of the laser and with the velocity. This is discussed by Mosedale *et al* [4], who used only a top-mounted detector system in measurements over a delta wing. Mosedale *et al* showed that the uncertainty was relatively constant, about 2 to 3 m s^{-1}, over a wide range of negative component frequencies, and all error terms contributed comparably. However, with Doppler shifts associated with positive frequency shifts, they found that the uncertainty increased markedly such that for a component velocity of 40 m s^{-1}, the uncertainty was $\sim$8 m s^{-1}. The reason for this increase in uncertainty is the reduction in the transmission–frequency sensitivity associated with these shifts. One observation that we can make from the bias values in table 1 is that our velocity detection limit is currently $\sim$1–2 m s^{-1} for frame-averaged velocities.

The measured bias and random errors associated with the empty tunnel measurements at the Mach 0.2 operating condition are reported in table 2. Here, Mach 0.2 corresponds to a tunnel axial velocity of 69.2 m s^{-1} and a component velocity of -18.9 m s^{-1} for the top-mounted detector. To compute the average velocity image, we used 130 individual images, though the actual number of images contributing to the averaged image varies with location in the field, due to inconsistent seeding in the wind tunnel. The measured bias and random errors were calculated by examining a cluster of approximately 21 000 pixels near the centre of the image, which were valid in both the instantaneous and averaged images. Note that pixels are considered invalid, as mentioned earlier, when signal levels in either the signal or reference cameras are too low or too high, or when the transmission ratios are too low or too high. The bias error, which was calculated in table 1, does not contain the uncertainty associated with Ω; when this is included, the total estimated uncertainty increases to 3.2 m s^{-1}. Of particular interest is the observation that the Doppler shift associated with a -18.9 m s^{-1} component velocity is only $\sim$60 MHz, which is comparable to the laser linewidth (estimated above to be $\sim$100 MHz). Indeed, based on the comparison between the empty-tunnel measurements and the independently measured value, we conclude that one can resolve frequency shifts much less than the laser linewidth.

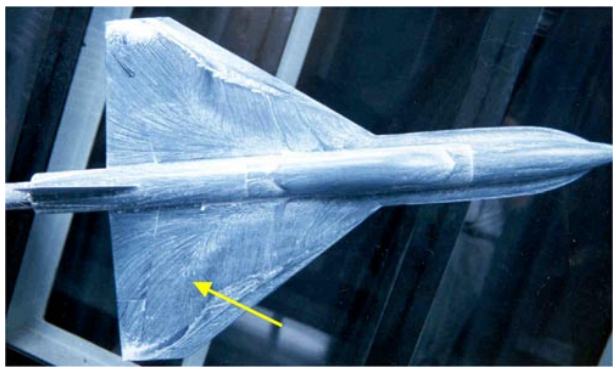

Figure 7. Oil flow visualization showing footprints of strake and wing leading-edge vortices. The burst point of the strake vortex is at approximately the location indicated by the arrow.

The random errors, taken here as a standard deviation of the velocities recorded over the region sampled in these images, were 0.95 m s^{-1} for the instantaneous case and 0.35 m s^{-1} for the averaged case. These errors are less than predicted by the uncertainty analysis outlined in table 1. Several factors may have contributed to this difference. First, the uncertainty analysis presented in table 1 may be somewhat conservative. For example, the noise in the signal and reference images was assumed to be uncorrelated, but included the effects of seeding variations, which should be removed in the processing procedure. Also, since only a small region of the image is analysed, the dominant bias error due to the variation of the angle ϕ over the image is reduced in comparison to the analysis of table 1. Table 2 also shows that the random error is reduced with frame averaging, from 0.95 to 0.35 m s^{-1}, though not as much as one might expect (i.e., not with the square root of the number of images). The reasons for this behaviour are not clear, though one possibility is that the 0.35 m s^{-1} error represents the residual speckle contribution of the flat-field correction, which is common to all the images. Also, the maximum number of individual images contributing to the frame-averaged image at any pixel location was 64—much less than the 130 total images taken—due to sparse seeding on individual images. Finally, note the decrease in the bias between the instantaneous (1.5 m s^{-1}) and frame-averaged error (1.0 m s^{-1}) in the tunnel velocity. All or part of this difference of 0.5 m s^{-1} may reflect the random error in the frequency monitoring system; indeed, from table 1 and the relative uncertainties in the photodiode signal intensities, $\Delta S_3/S_3$ and $\Delta S_4/S_4$, we would estimate that the uncertainty associated with the derived laser frequency is $\sim$0.3 m s^{-1}.

Relative to previous investigations, the errors associated with the iodine cell transmission characteristics have been reduced by use of a starved iodine cell. Currently, the greatest bias uncertainty is associated with the variation in the angle ϕ across the image. Of course, this is a relatively simple uncertainty to eliminate in post-processing, since the variation of ϕ across the image is known, although only the centreline value is used here. However, this points out an important aspect of the PDV measurements—namely that the measured velocity component varies slightly across the image. The largest

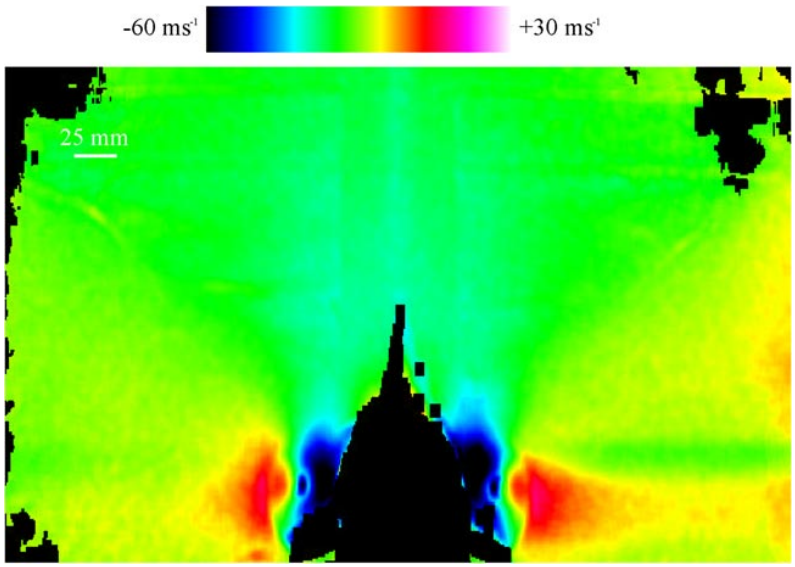

Figure 8. Frame-averaged PDV measurements with the top-mounted detector at a location 108 mm forward of the wing/strake junction. The measured velocity component is in the $(-0.253\boldsymbol{i}, 0.0\boldsymbol{j}, 0.968\boldsymbol{k})$ direction. The strake surface corresponds to the bottom of the image, and the view is full span. Local saturation from reflections off the model has caused data drop-out in regions directly over the strake and curved model body in this image and those that follow; these areas are shown in black in the figure.

random uncertainty in the velocity arises from uncertainties in the intensities of the signal and reference cameras. As reported earlier, this error is due primarily to speckle noise. Although reduced by using a low-f-number lens, low-pass filtering and multiple-image averaging (for a time-averaged result), speckle still dominates the random uncertainty.

In the empty-tunnel error analysis, errors associated with surface reflections off the model have not been considered. Secondary scattering off model surfaces may result in diffuse illumination of the seed particles in the flow, resulting in scattering by particles not in the plane of the light sheet. Local saturation in an image may also result if the laser sheet impinges on the model and if this impingement is within the camera field of view. This type of secondary scattering may be reduced by painting the model with flat black paint, as was done in these experiments, or by aligning the laser sheet so as to avoid direct impingement on the model surfaces. In this experiment, the location of the vortices of interest and the geometry of the model made direct impingement of the light sheet on the strake, wing and fuselage of the model unavoidable. This resulted in areas of saturation in the cameras image immediately above the model surface (see section 5). Another type of secondary scattering results when a model surface is within the field of view, directly behind the light sheet. This type of scattering may be observed in the data presented here, for example, in the tail reflections in figures 12–15. In this case, the tail reflected light scattered from the light sheet, resulting in a bias error in the data. This bias error is localized in the image, and, of course, is dependent on the model geometry and optical configuration. In this case, the bias error due to these tail reflections could be estimated by comparing the velocity measurements in the vicinity of the reflection to those directly corresponding to the reflection location. The surface reflections on the tail were estimated to produce a bias error of ~ -6 m s^{-1} in these images

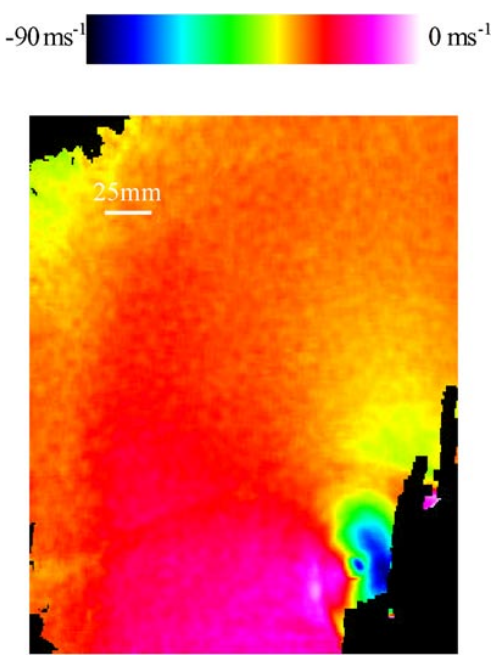

Figure 9. Frame-averaged PDV measurements with the side-mounted detector at the same axial location as in figure 8. The measured velocity component is in the $(-0.296\boldsymbol{i}, 0.421\boldsymbol{j}, 0.857\boldsymbol{k})$ direction. The model body obstructed the view of the right side of the model, resulting in a semi-span field of view. The bottom of the image corresponds to the strake surface, while the right side of the image corresponds to the model centreline.

5. Wind tunnel measurements over the model aircraft

For measurements around the 56° delta wing model, two light-sheet inclinations were used. With the two forward locations on the model (A and B in figure 6), the fields of view and light sheet were centred on the model centreline. However, due to

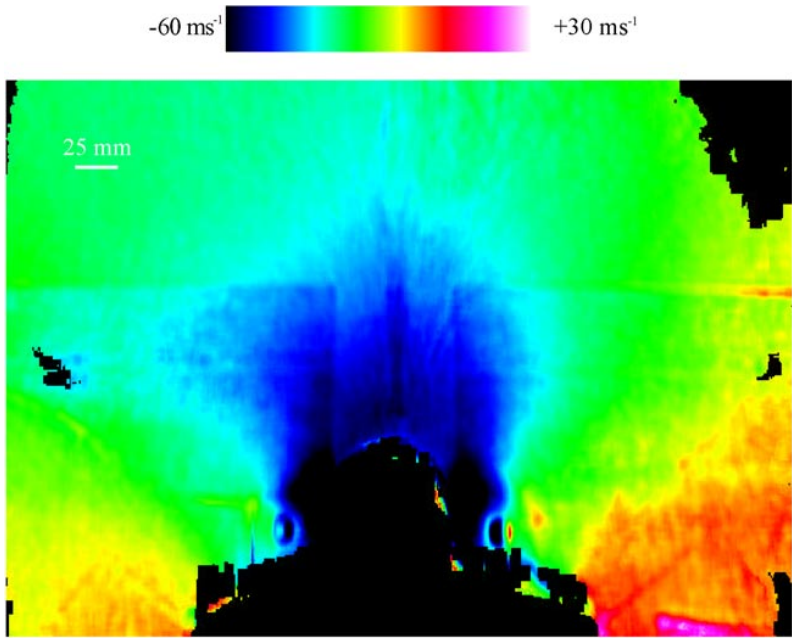

Figure 10. Frame-averaged PDV measurements with the top-mounted detector at a location 76 mm downstream of the wing/strake junction. The measured velocity component is in the $(-0.253\boldsymbol{i}, 0.0\boldsymbol{j}, 0.968\boldsymbol{k})$ direction. The wing surface corresponds to the bottom of the image, and the view is full span.

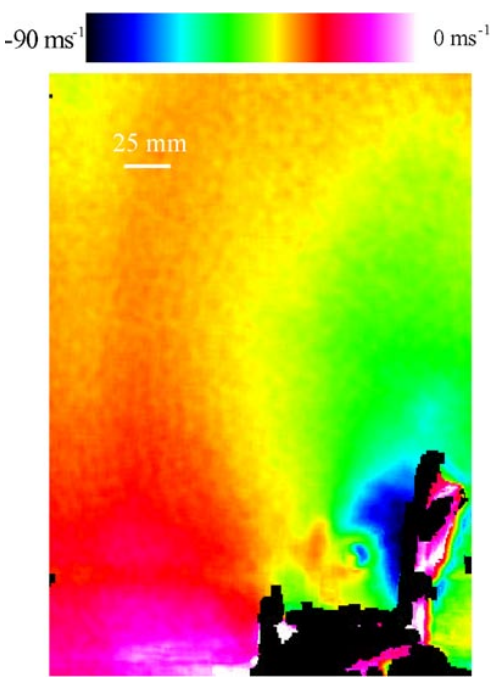

Figure 11. Frame-averaged PDV measurements with the side-mounted detector at the same axial location as in figure 10. The measured velocity component is in the $(-0.296\boldsymbol{i}, 0.421\boldsymbol{j}, 0.857\boldsymbol{k})$ direction. As in figure 9, the model body obscures the view of the strake vortex on the right side of the model, resulting in a semi-span image. The bottom of the image corresponds to the wing surface, while the right side of the image corresponds to the model centreline.

obstructions from the model body, the side-mounted detector could only view the vortex on one side of the model. Due to optical access limitations, the light sheets in these cases were inclined 7° upstream to a plane normal to the model body axis, as described earlier. At the forward locations, the PDV cameras on top of the tunnel were sensitive to a nominal velocity component in the direction $(-0.253\hat{\boldsymbol{i}}, 0.0\hat{\boldsymbol{j}}, 0.968\hat{\boldsymbol{k}})$, where $\hat{\boldsymbol{i}}$, $\hat{\boldsymbol{j}}$ and $\hat{\boldsymbol{k}}$ are unit vectors in the wind-tunnel-frame downstream, spanwise and upward directions, respectively. The side-mounted detector was sensitive to a velocity component in the direction $(-0.296\hat{\boldsymbol{i}}, 0.421\hat{\boldsymbol{j}}, 0.857\hat{\boldsymbol{k}})$.

For the two downstream locations (C and D in figure 6), the light sheet was inclined normal to the model body axis and the light sheet and cameras were centred on the left side of the model (looking downstream), with slightly better than semi-span coverage of the model. This configuration allowed us to make measurements of the strake vortex on both sides of the model with the top-mounted detector, which was sensitive to a velocity component in the direction $(-0.225\hat{\boldsymbol{i}}, 0.0\hat{\boldsymbol{j}}, 0.974\hat{\boldsymbol{k}})$. With the side-mounted detector, which was sensitive to a velocity component in the $(-0.278\hat{\boldsymbol{i}}, 0.386\hat{\boldsymbol{j}}, 0.880\hat{\boldsymbol{k}})$ direction, we could record only semi-span data; since the view of the strake vortex on the right side of the model was obscured by the model body.

Figure 7 shows surface oil flow visualization on the model. In this figure, the footprints of both the strake and leading edge vortices can be seen. The outboard turn of the strake vortex is noticeable in this figure, and the approximate burst location, based on observation of condensation in the vortex core, is marked in the figure. Figures 8 and 9 show velocities from the respective top-mounted and side-mounted detectors at the most upstream measurement location, 108 mm upstream of the wing/strake junction. Local saturation from model reflections (recall the laser sheet originating from the top of the tunnel is striking the model directly) causes data drop-out in regions directly over the strake and curved model body. In spite of the limitations imposed by CCD saturation, strong strake vortices (one on either side of the model) can be seen clearly in the images. Figures 10 and 11 show similar data

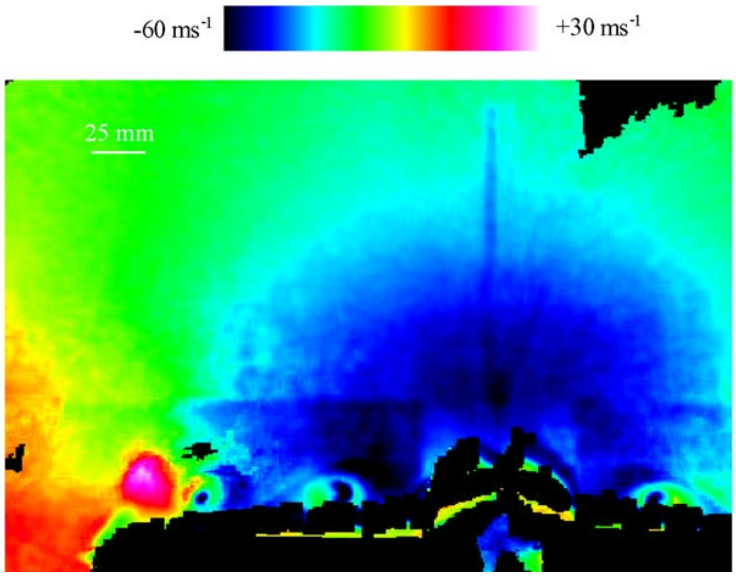

Figure 12. Frame-averaged PDV measurements with the top-mounted detector at a location corresponding to the trailing dge of the canopy. The measured velocity component is in the $(-0.225\boldsymbol{i}, 0.0\boldsymbol{j}, 0.974\boldsymbol{k})$ direction. The wing surface corresponds to the bottom of the image, and the field of view is slightly greater than semi-span, with the reflections off the vertical tail marking the centreline of the model. Model reflections such as these caused a bias error of approximately 6 m s^{-1} in the measured velocity.

at the next measurement location, 76 mm downstream of the wing/strake junction. The strake vortices still appear in these images, although they have begun to move outboard under the influence of the wing flow field. Figures 12 and 13 show similar data at the next measurement location, corresponding to the trailing edge of the canopy on the model. As noted earlier, the measurement plane is shifted to the left side (looking downstream) of the model in these figures as well as the next two figures. Again, local saturation limits the data collection near the model surface, corresponding to the bottom of the image. In addition, reflections off the tail leading edge mark the centreline of the model with a vertical line in images recorded with the top-mounted detector; in images from the side-mounted detector, these reflections appear as a diagonal line. A weakened, outboard turning strake vortex can be seen in these images, and a stronger wing vortex has also developed by this axial station. Figures 14 and 15 show similar data at the next measurement location, corresponding to the leading edge of the wing tip. The strake vortex has burst by this location, after having turned outboard, and thus does not show up in figures 14 or 15.

Taken in total, these images capture the formation of the strake vortex, its outboard migration over the wing and its eventual burst over the wing. The strake and leading-edge vortices tend to twist due to their interaction as they move downstream. While the strake vortex turns outboard over the wing, it is held close to the surface due to the interaction with the wing leading edge vortex. In turn, the strake vortex tends to lift the wing leading edge vortex off the wing surface. The growth of the wing leading-edge vortex, in both strength and core diameter, can also be seen in the last two sets of figures (figures 12–15). These results are particularly interesting because they have captured the complex interaction of multiple vortices in the presence of the wing flow field, and the measurements were made on a realistic geometry with complicating geometric features that are characteristic of a realistic fighter geometry.

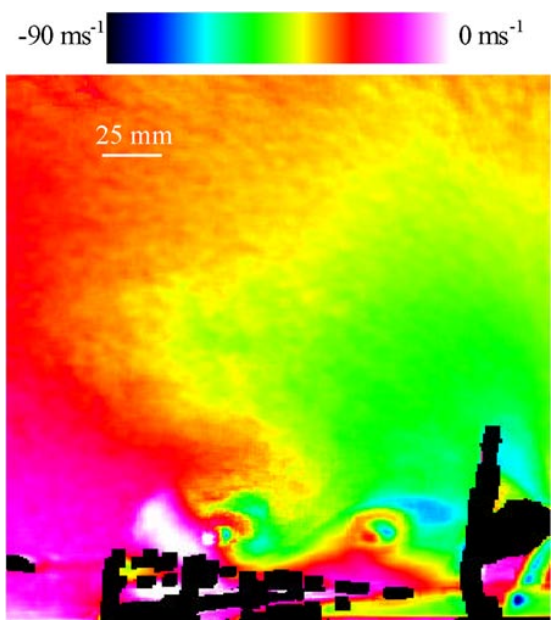

Figure 13. Frame-averaged PDV measurements with the side-mounted detector at the same axial location as in figure 12. The measured velocity component is in the direction $(-0.278\boldsymbol{i}, 0.386\boldsymbol{j}, 0.880\boldsymbol{k})$. The wing surface corresponds to the bottom of the image, while the centreline of the model corresponds to the right side of the image. As with the other measurements with the side-mounted system, the data shown are for a semi-span field of view.

6. Conclusions

We have demonstrated the power of the PDV technique by employing it in a large-scale wind tunnel to record planar

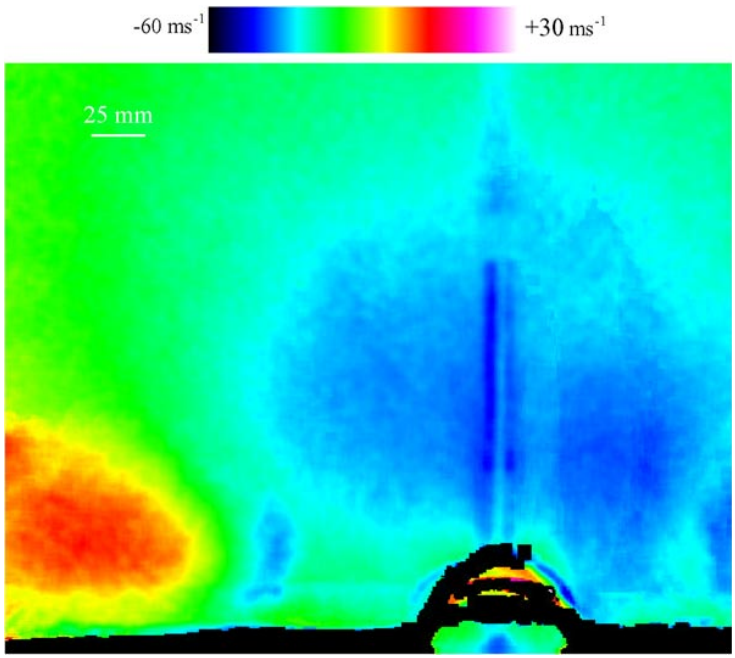

Figure 14. Frame-averaged PDV measurements with the top-mounted detector at a location corresponding to the leading edge of the wing tip. The measured velocity component is in the $(-0.225\boldsymbol{i}, 0.0\boldsymbol{j}, 0.974\boldsymbol{k})$ direction, and the field of view is slightly greater than semi-span, with the reflections off the tail marking the model centreline. The wing surface corresponds to the bottom of this image.

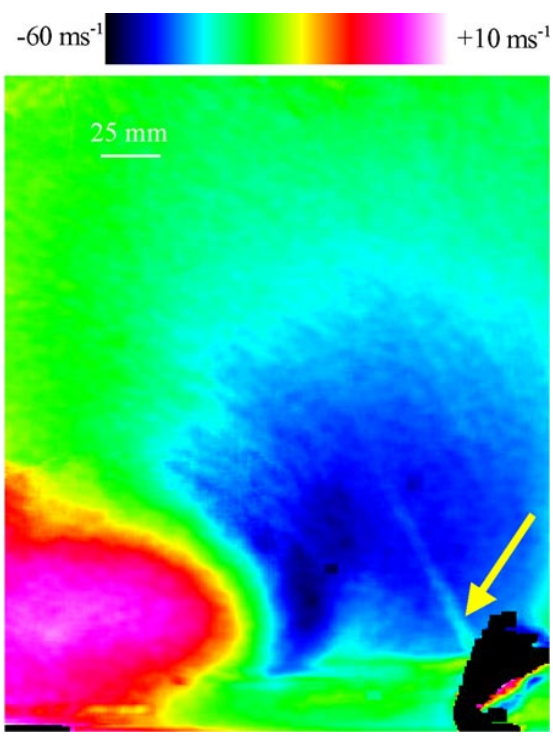

Figure 15. Frame-averaged PDV measurements with the top-mounted detector at the same axial location as in figure 14. The measured velocity component is in the direction $(-0.278\boldsymbol{i}, 0.386\boldsymbol{j}, 0.880\boldsymbol{k})$. The field of view is semi-span, with the wing surface corresponding to the bottom of the image and the model centreline corresponding to the right side of the image. The tail reflections, identified by the arrow, appear in this view as a diagonal line.

velocity fields surrounding a model of a generic fighter plane. In particular, velocity images recorded at four planes along the model have shown the formation and interaction of forebody and leading-edge vortices. The PDV instrument employed here included (i) a frequency monitoring system for measuring the laser frequency with each laser pulse, (ii) two detector stations (one viewing the model from the top of the wind tunnel and the second from the side); (iii) *starved* iodine vapour cells, (iv) a vibration-isolated Nd:YAG laser and (v) custom data acquisition software. To validate the PDV instrument, we compared the PDV-derived velocity to the known value in the empty wind tunnel (that is, with the model removed). Here, we found an error of about 1 m s^{-1} out of an 18.9 m s^{-1} component velocity. The noise component in the instantaneous smoothed images, which results primarily from the speckle effect, was found to be ∼1–2 m s^{-1}.

Several improvements to the PDV technique have been implemented and recommendations for future applications include the following.

(1) The use of starved iodine cells eliminates the requirement for precise cold-finger temperature control during operation of the PDV system in harsh wind-tunnel environments. The use of permanently sealed starved cells (which have now been fabricated) may further reduce repetitive calibrations, system checks and bias errors associated with the cell conditions.

(2) Vibration isolation of the laser is essential to reduce the number of multi-mode pulses when operating in high-noise, high-vibration environments. Ideally, vibration isolation should be performed on an entire optical table containing the laser and the frequency monitoring system. Furthermore, pneumatic isolation alone of the optical table is not ideal; the position of the table should be accurately controlled to prevent laser-beam wander relative to the model. Even with isolation and position control, however,

the laser must be monitored for frequency shifts and single frequency operation on a pulse-by-pulse basis.

(3) Laser speckle remains a dominant random error source in the PDV system. For the measurement of time-resolved velocities, speckle noise may be reduced by means of hardware modifications—e.g. larger lens aperture and larger detector size—and low-pass filtering. Of course, frame averaging is also effective in reducing speckle noise for the recording of time-averaged velocities.

(4) When possible, light sheets and cameras should be oriented to avoid direct impingement of the light sheet on model surfaces within the field of view of the cameras. Complex model geometry often limits the orientations of both the light sheet and detectors, however, resulting in unavoidable areas of saturation in the images and regions of bias from secondary scattering.

(5) Detailed calibration procedures, including flat-field corrections, tie-point mapping, background subtraction and periodic checks on iodine cell performance, must be incorporated in the data collection and processing. The ability to validate/check system operation—e.g. by performing *in situ* calibration by recording images with the laser tuned out of the absorption profile, measuring known velocity fields and monitoring the laser operating frequency—is essential.

Overall, the PDV technique has advanced to the point that it may be used to make reliable, multi-component velocity measurements of complex flow fields in large-scale facilities. Though issues such as background scattering and speckle continue to affect the overall system performance, PDV enables the mapping of high-spatial-resolution velocity fields over complex models in a relatively short period of time. This technique may be used both to guide the development of future aircraft, and as a means of providing detailed flow-field measurements for the development of CFD methods.

Acknowledgments

The authors gratefully acknowledge the help of Dr William Weaver in the development of data acquisition programs. This work was supported in part by a Small Business Innovative Research (SBIR) contract with Innovative Scientific Solutions, Inc. Professor Elliott would also like to acknowledge the support of the National Science Foundation (NSF: 9733388), Dr Chuan Chen, monitor. The authors gratefully acknowledge the use of iodine spectrum codes provided by J Forkey of Princeton University.

References

[1] McKenzie R L 1995 Measurement capabilities of planar Doppler velocimetry using pulsed lasers *33rd Aerospace Sciences Meeting (Reno, NV, 1995) AIAA Paper* 95-0297

[2] Mosedale A D, Elliott G S, Carter C D and Beutner T J 1998 Planar Doppler velocimetry: toward turbulence measurements *Proc. FEDSM '98 ASME Fluids Eng. Div. Summer Meeting (Washington, DC)* paper FEDSM98-5088

[3] McKenzie R L 1997 Planar Doppler velocimetry for large-scale wind tunnel applications *35th Aerospace Sciences Meeting (Reno, NV, 1997) AIAA Paper* 97-0498

[4] Mosedale A D, Elliott G S, Carter C D and Beutner T J 2000 Planar Doppler velocimetry in a large-scale facility *AIAA J.* **38** 1010–24

[5] Clancy P S and Samimy M 1997 Multiple-component velocimetry in high speed flows using planar Doppler velocimetry *35th Aerospace Sciences Meeting (Reno, NV, 1997) AIAA Paper* 97-0497

[6] Clancy P S, Samimy M and Erskine W R 1998 Planar Doppler velocimetry: three component velocimetry in supersonic jets *36th Aerospace Sciences Meeting (Reno, NV, 1997) AIAA Paper* 98-0506

[7] Smith M W 1998 Application of a planar Doppler velocimetry system to a high reynolds number compressible jet *36th Aerospace Sciences Meeting (Reno, NV, 1997) AIAA Paper* 98-0428

[8] Smith M W and Northam G B 1995 Application of absorption filter-planar Doppler velocimetry to sonic and supersonic jets *33rd Aerospace Sciences Meeting (Reno, NV, 1995) AIAA Paper* 95-0299

[9] Smith M W 1998 The reduction of laser speckle noise in planar Doppler velocimetry systems *20th Advanced Measurement and Ground Testing Conf. (Albuquerque, NM, 1998) AIAA paper* 98-2607

[10] Forkey J N, Finkelstein N D, Lempert W R and Miles R B 1996 Demonstration and characterization of filtered Rayleigh scattering for planar velocity measurements *AIAA J.* **34** 442–8

[11] Miles R B, Forkey J N and Lempert W R 1992 Filtered Rayleigh scattering measurements in supersonic/hypersonic facilities *17th Aerospace Ground Testing Conf. (Nashville, TN, 1992) AIAA Paper* 92-3894

[12] Forkey J N 1996 Development and demonstration of filtered Rayleigh scattering—a laser based flow diagnostic for planar measurement of velocity, temperature and pressure *Princeton University Department of Mechanical and Aerospace Engineering Technical Report* 2067

[13] Miles R B, Lempert W R and Forkey J N 1991 Instantaneous velocity fields and background suppression by filtered Rayleigh scattering *29th Aerospace Sciences Meeting (Reno, NV, 1991) AIAA Paper* 91-0357

[14] Beutner T J, Williams G W, Baust H D, Elliott G S, Crafton J and Carter C D 1999 Characterization and applications of Doppler global velocimetry *37th Aerospace Sciences Meeting (Reno, NV, 1999) AIAA Paper* 99-0266

[15] Komine H, Brosnan S J, Litton A B and Stappaerts E A 1991 Real-time, Doppler global velocimetry *29th Aerospace Sciences Meeting (Reno, NV, 1991) AIAA Paper* 91-0337

[16] Komine H and Brosnan S J 1991 Instantaneous, three component, Doppler global velocimetry *Laser Anemometry* **1** 273–7

[17] Meyers J F and Komine H 1991 Doppler global velocimetry: a new way to look at velocity *Laser Anemometry* **1** 289–96

[18] Meyers J F 1994 Development of Doppler global velocimetry for wind tunnel testing *18th Aerospace Ground Testing Conf. (Colorado Springs, CO, 1994) AIAA Paper* 94-2582

[19] Beutner T J, Baust H D and Meyers J F 1995 Doppler global velocimetry measurements of a vortex-tail interaction *Proc. 7th Int. Symp. on Flow Visualization (Seattle, WA, 1995)*

[20] Meyers J F 1996 Evolution of Doppler global velocimetry data processing *8th Int. Symp. on Applications of Laser Techniques to Fluid Mechanics (Lisbon, 1996)*

[21] Meyers J F, Lee J W, Fletcher M T and South B W 1998 Hardening Doppler global velocimetry systems for large wind tunnel applications *20th AIAA Advanced Measurement and Ground Testing Conf. (Albuquerque, NM, 1998) AIAA Paper* 98-2606

[22] Naylor S and Kuhlman J 1998 Accuracy studies of a two-component Doppler global velocimeter (DGV) *36th Aerospace Sciences Meeting (Reno, NV, 1998) AIAA Paper* 98-0508

[23] Beutner T J, Elliott G, Mosedale A and Carter C 1998 Doppler global velocimetry applications in large scale facilities *20th Advanced Measurement and Ground Testing Conf. (Albuquerque, NM, 1998) AIAA Paper* 98-2608
[24] Roehle I 1996 Three-dimensional Doppler global velocimetry in the flow of a fuel spray nozzle and in the wake region of a car *Flow Meas. Instrum.* **7** 287–94
[25] Roehle I 1999 *Doppler Global Velocimetry* RTO-EN-6, pp 4.1–4.22
[26] Beutner T J and Baust H D 1997 Recent developments in Doppler global velocimetry *AGARD/RTO Conf. Proc.* CP-601, Paper 8
[27] Reinath M S 1997 *Doppler Global Velocimetry Development for the Large Wind Tunnels at Ames Research Center* NASA TM 112210
[28] Arnette S A, Samimy M and Elliott G S 1996 Two-component filtered planar velocimetry in the compressible turbulent boundary layer *34th Aerospace Sciences Meeting (Reno, NV, 1996) AIAA Paper* 96-0305
[29] Elliott G S and Beutner T J 1999 Molecular filter based planar Doppler velocimetry *Prog. Aerospace Sci.* **35** 799–845
[30] Samimy M and Wernet M P 2000 Review of planar multiple-component velocimetry in high-speed flows *AIAA J.* **38** 553–74
[31] Shimizu H, Lee S and She C 1983 High spectral resolution lidar system with atomic blocking filters for measuring atmospheric parameters *Appl. Opt.* **22** 1373–81
[32] Shimizu H, Noguchi I and She C 1986 Atmospheric temperature measurement by high spectral resolution LIDAR *Appl. Opt.* **25** 1460–6
[33] Elliott G S 1993 A study of compressible mixing layers using laser based diagnostic techniques *PhD Dissertation* Department of Mechanical Engineering, The Ohio State University
[34] Elliott G S, Samimy M and Arnette S A 1994 A molecular filter based velocimetry technique for high speed flows *Exp. Fluids* **18** 107–18
[35] Arnette S A, Samimy M and Elliott G S 1998 Two component planar Doppler velocimetry in the compressible turbulent boundary layer *Exp. Fluids* **14** 232–332
[36] Smith M W, Northam G B and Drummond J P 1996 Application of absorption filter planar Doppler velocimetry to sonic and supersonic jets *AIAIA J.* **34** 434–41
[37] Arnette S A, Elliott G S, Mosedale A D and Carter C D 2000 Two-color planar Doppler velocimetry *AIAA J.* **38** 2001–6
[38] Spectra-Physics 1996 *Pulsed Nd:YAG Lasers, User's Manual, GCR Series*
[39] Spectra-Physics 1994 *Model 6350 Instruction Manual*
[40] PixelVision 1996 *User's Manual SpectraVideo*™ *Camera*
[41] Melles Griot 1990 *Optics Guide 5* p 13.10
[42] Thor Labs 1996 High-speed silicon detector—DET200 *Thor Labs Data Sheet*
[43] Stanford Research Systems 1993 *Fast Gated Integrators and Boxcar Averagers*
[44] Tellinghuisen J 1982 Transition strengths in the visible-infrared absorption spectrum of I_2 *J. Chem. Phys.* **76** 4736–43
[45] Gogineni S, Goss L and Beutner T 1999 Application of two-color PIV in a large scale wind tunnel facility *37th AIAA Aerospace Sciences Meeting (Reno, NV, 1999) AIAA Paper* 99-0269